

Quantifying CH₄ emissions from coal mine aggregation areas in Shanxi, China using TROPOMI observations and the wind-assigned anomaly method

Qiansi Tu¹, Frank Hase², Kai Qin³, Jason Blake Cohen³, Farahnaz Khosrawi⁴, Xinrui Zou¹, Matthias Schneider¹, Fan Lu³

¹Tongji University, School of Mechanical Engineering, Shanghai, China

²Karlsruhe Institute of Technology (KIT), Institute of Meteorology and Climate Research (IMK-ASF), Karlsruhe, Germany

³China University of Mining and Technology, School of Environment and Spatial Informatics, Xuzhou, China

⁴Forschungszentrum Jülich GmbH, Jülich Supercomputing Centre (JSC), Jülich, Germany

10 Correspondence to: Qiansi Tu (tuqiansi@tongji.edu.cn), Kai Qin (qinkai@cumt.edu.cn)

Abstract.

China stands out as a major contributor to anthropogenic methane (CH₄) emissions, with coal mine methane (CMM) playing a crucial role. To control and reduce CH₄ emissions, China has made a dedicated commitment and formulated an ambitious mitigation plan. To verify the ~~process~~ progress made, the consistent acquisition of independent CH₄ emission data is required. This paper aims to implement a wind-assigned anomaly method for the precise determination of regional-scale CMM emissions within the coal-rich Shanxi province. We use the Tropospheric Monitoring Instrument (TROPOMI) CH₄ observations from May 2018 to May 2023, coupled with ERA5 wind ~~covering the Changzhi, Jincheng and Yangquan regions~~ and a bottom-up inventory dataset based on the IPCC Tier 2 approach covering the Changzhi, Jincheng and Yangquan regions of the Shanxi province. The derived emission strengths are $8.4 \times 10^{26} \pm 1.6 \times 10^{25}$ -molec. s⁻¹ (0.706 ± 0.013 -Tg yr⁻¹, $\pm 25\%$), $1.4 \times 10^{27} \pm 1.9 \times 10^{25}$ -molec. s⁻¹ (1.176 ± 0.016 -Tg yr⁻¹, $\pm 20\%$), and $4.9 \times 10^{26} \pm 1.8 \times 10^{25}$ -molec. s⁻¹ (0.412 ± 0.015 -Tg yr⁻¹, $\pm 21\%$), respectively. Our results exhibit biases of -18%, 8%, and 14%, respectively, when compared to the IPCC Tier 2 bottom-up inventory. Larger discrepancies are found when comparing the estimates to the CAMS-GLOB-ANT and EDGARv7.0 inventories (64%-176%), suggesting that the two inventories may be overestimating ~~the~~ CH₄ emissions from the studied coal mining regions. Our estimates provide a comprehensive characterization of the regions within the Shanxi province, contribute to the validation of emission inventories, and ~~help~~ provide additional insights into CMM emissions mitigation. ~~develop climate mitigation strategies.~~

1. Introduction

Methane (CH₄) is the second most important anthropogenic greenhouse gas (GHG) with a relatively shorter lifetime but a larger global warming potential than carbon dioxide (CO₂) (IPCC, 2014; Etminan et al., 2016). For this reason, efforts to reduce CH₄ emissions would be beneficial for rapid climate change mitigation in the short term. The atmospheric CH₄ is

emitted from a variety of natural sources (accounting for 40%, [e.g.](#), wetlands, termites) and anthropogenic sources (accounting for 60%, [e.g.](#) industrial fossil fuel production and consumption, waste disposal, agriculture) (Saunio et al., 2020). Currently, a significant fraction (~33% for the 2008-2017 decade) of global CH₄ emissions related to fossil fuels comes from the exploitation, transportation, and usage of coal (Saunio et al., 2020). China is one of the leading CH₄ emitters in the world and accounted for around 14-22% of global anthropogenic CH₄ emission (Janssens-Maenhout et al., 2019; Liu et al., 2021). [China has demonstrated its commitment to addressing CH₄ emissions by signing key international agreements such as the Kyoto Protocol in 1998 and the Paris Agreement in 2016, underscoring its commitment to global efforts in mitigating climate change.](#) [Additionally, in 2021, China ~~pledged~~ committed to reduce CH₄ emissions under the Glasgow Agreement and intended to develop a comprehensive and ambitious National Action Plan with the goal of achieving a substantial impact on methane emissions control and reductions in the 2020s \(USDoS, 2021\).](#) Thus, the precise measurement of CH₄ emission changes is essential for determining the effectiveness of these commitments.

The anthropogenic CH₄ emissions in China increased by 40% in the 2000s (Liu et al., 2021), probably reflecting increasing coal production (Gao et al., 2021). Coal production in China reached 3.9 Gt in 2020, with approximately half of the coal being utilized for thermal power generation (National Bureau of Statistics of China, 2022). China's official GHG emission inventory (MEE, 2019) reports that the country's coal mine methane (CMM) emissions amounted to about 21 Tg in 2014, thus accounting for 38% of its total anthropogenic CH₄ emissions. China has submitted three versions of the National Communications on Climate Change (NDRC, 2004, 2012; MEE, 2019b) and two reports of Biennial Update Reports on Climate Change since 2004 (NDRC, 2017; MEE 2019a), in which the estimated inventories of the CMM emissions are reported. The current CMM emission inventories are usually based on bottom-up data-based approaches, which involves identifying and quantifying the CH₄ emissions from each type of coal mine (Gao et al., 2020).

Mainland China's coal mines are spread across 26 provinces and were comprised of approximately 1000 coalfields and over 10,000 coal mines in 2011 (SACMS, 2012). The CMM emissions in China show unique characteristics and complexities, due to the large variability of the coal rank, capacity, geological conditions, and mining technologies of the numerous coal mines (Gao et al., 2020, 2021; Peng et al., 2016; Scarpelli et al., 2020). This large number of coal mines and the heterogeneity between them also induce considerable uncertainties in bottom-up estimates and ~~so~~ are [thus](#) a challenge in achieving accurate CMM emissions [estimates](#) (Sheng et al., 2019). [Qu et al. \(2021\) highlighted significant challenges in their satellite inversion over southeast China characterized by elevated seasonal rice emissions that coincide with extensive cloud cover and potential misallocation of coal emission. A recent study from Chen et al. \(2022\) suggests a downward correction in CMM emissions \(-15%\) in China compared to the United Nations Framework Convention on Climate Change \(UNFCCC\) reports, partly driven by reductions in the Shanxi province. Zhang et al. \(2021\) documented an overestimation of anthropogenic emissions from China, revealing a 30% decrease in the posterior estimates, with approximately 60% of this downward correction attributed to coal mining.](#) Therefore, a strong demand exists for independent and objective verification of CMM emissions from local to regional scales based on atmospheric observations, which are commonly known as top-down approaches. The observations from

satellites, e.g. the TROPospheric Monitoring Instrument (TROPOMI) on board the Sentinel-5 Precursor satellite, provide [due to their global, high-resolution measurements](#), the ability to estimate the CMM emissions ~~on both global and from~~ regional scales (Sadavarte et al., 2021; Tu et al., 2022b; Chen et al., 2022) [to a global scale](#) (Shen et al., 2023).

This study conducts the wind-assigned anomaly method (Tu et al., 2022a, b) on TROPOMI XCH₄ observations [derived](#) from 2018 to 2023 ~~over for~~ three subregions in [the](#) Shanxi province to determine the CMM emissions over that period. Shanxi province is known for its abundant coal reserves and is considered one of the coal-richest provinces in China. The coal production in Shanxi exceeded 1 billion tons in 2021, accounting for nearly one-third of the country's total coal output and 12% of the global output. This highlights the significant role of Shanxi province in China's energy sector and emphasizes the importance of estimating CMM emissions from the mining activities in the region. In this work, the emission estimation method and the TROPOMI dataset are introduced in Sect. 2. In Sect. 3 we present the results of the TROPOMI observations and three different inventories used for comparison, followed by estimated CMM emissions over three subregions. An uncertainty analysis based on a dispersion model, wind information and inventory ~~is~~[are](#) also performed in this section. A conclusion is given in Sect. 4.

2. Data and method

2.1 TROPOMI dataset

Launched in October 2017, the TROPOMI instrument is an imaging spectrometer which is designed to view the Earth in nadir direction. The instrument utilizes passive remote-sensing techniques to measure [the backscattered solar radiation](#) ~~solar radiation reflected by and radiated from the Earth~~ across the ultraviolet (UV), visible (VIS), near-infrared (NIR), and short-wave spectral (SWIR) bands (Veefkind et al., 2012). The instrument is capable of providing an unprecedented [combination of](#) high spatial resolution ($5.5 \times 7 \text{ km}^2$) and complete daily global coverage of the CH₄ total column-averaged dry-air mole fraction (XCH₄) (Veefkind et al., 2012; Lorente et al., 2021). The RemoTec algorithm, which has been widely utilized in deriving CH₄ and CO₂ from the Greenhouse Gases Observing Satellite (GOSAT) (Butz et al., 2011; Guerlet et al., 2013), is also deployed here to retrieve XCH₄ from TROPOMI measurements. These measurements capture sunlight backscattered by the Earth's surface and atmosphere in the NIR and SWIR spectral bands (Hu et al., 2018). Recent studies show the potential of using high-resolution TROPOMI XCH₄ for detection and quantification of the CH₄ emissions. TROPOMI observations have been used for quantifying CH₄ emissions from the oil and gas sector (Pandey et al., 2019; Varon et al., 2019; de Gouw et al., 2020; Schneising et al., 2020; Zhang et al., 2020), from urban areas (Tu et al., 2022a; Foy et al., 2023; Plant et al., 2022), and from coal mining (Sadavarte et al., 2021; Tu et al., 2022b). In this study, the TROPOMI XCH₄ observations spanning the period from May 2018 to May 2023 over the study areas in the Shanxi province are used. [A data quality filter \(qa = 1.0\) is applied to characterize the data during clear-sky and low-cloud atmospheric conditions.](#)

2.2 CH₄ inventory datasets

95 Qin et al. (2023) used both public and private datasets from over 600 individual coal mines in Shanxi Province. The IPCC
Tier 2 approach is applied to calculate the corresponding CH₄ emissions based on 3-5 sets of observed emission factors, thereby
establishing a range of bottom-up estimation of CMM on a mine-by-mine basis. In the following work, the bottom-up inventory
computed from the median emission factors (E5) will serve as a prior information in the wind-assigned method for estimating
emissions, referring to IPCC Tier 2 bottom-up inventory. In their study, an eddy-covariance tower was installed in Changzhi
100 during two two-month periods to derive an average observed CH₄ flux. Based on the in-situ measurements, a series of scaling
factors at different percentiles of the observational distribution (i.e., 10%, 30%, 50%, 70%, 90%) were generated. These scaling
factors were subsequently employed to update the preliminary Tier 2 bottom-up inventory (Qin et al., 2023). The scaling
factors for a specific percentile of the observational distribution show minimal variations among different coal mines,
suggesting these factors can be treated as constant values across the ensemble of coal mines at each percentile. Our wind-
105 assigned method emphasizes the proportional share of emissions per mine rather than absolute values, resulting in estimated
CMM emissions that do not significantly differ whether using the Tier 2 bottom-up inventory or one of the scaled inventory
datasets. In addition to the current IPCC 2 Tier bottom-up inventory, the scaled inventory is also provided as an additional
reference point in this work.

110 The CAMS Global anthropogenic emissions (CAMS-GLOB-ANT) inventory provides methane emissions for different
sectors with a spatial resolution of 0.1° × 0.1° and temporal coverage from 2000 to 2024 (Granier et al., 2019;
<https://permalink.aeris-data.fr/CAMS-GLOB-ANT>, last access: 12 July 2023). Emissions are provided as monthly and yearly
averages and v5.3, which includes updated ship emissions from CAMS-GLOB-SHIP v3.1, is used in this study. The yearly
mean of CAMS-GLOB-ANT for 14 sectors are illustrated in Figure 1a. Emissions from maritime transport in the study area
are zero and not shown here. The inventory very well presents the dominant emission sources in the study area. The coal
115 production (fugitives (coal)) is the dominant source of methane emissions, accounting for ~96% of the ~~in~~ total emissions. The
sector of solid waste and waste water is the ~~secondary~~ second most important emission source which ~~drops~~ contributes to 2%.
Figure 1b shows the spatial distribution of coal emission in Changzhi and the corresponding distributions for Jincheng and
Yangquan are presented in Figure A- 1. The locations of the coal mines and the corresponding emission rates ~~fit well~~ are in
good agreement with the CAMS inventory. About half of the coal mines are concentrated in the southern region, while the
120 other half are located further north, along a southwest to northeast direction. The two reddish grids points (36.05°N-36.15°N,
113.05°E) denote the highest emission rate in the CAMS inventory, partly due to the Changzhi city, which is located nearby.
The CH₄ emission in the city region are primarily attributed to the traffic (particularly during the morning and evening rush
hours), CH₄ leaks at gas stations and is released by the utilization and release of natural gas in residential areas (Liu et al.,
2022). The CH₄ emission accounts for 1.77×10^{27} molec. s⁻¹ (1.5 Tg yr⁻¹) for the whole study area, which is 55% higher than
125 the IPCC Tier 2 bottom-up inventory (1.14×10^{27} molec. s⁻¹ ~ 0.96 Tg yr⁻¹).

The EDGARv7.0 emission inventory is the first product of the new Emissions Database for Global Atmospheric Research (EDGAR) Community GHG emissions database (Crippa et al., 2021), which provides estimates of emissions of the three main GHGs (CO₂, CH₄ and N₂O) and fluorinated gases per sector and country. The dataset offers the same spatial resolution of 0.1° × 0.1° as the CAMS inventory and covers the period of 1970 to 2022. The CH₄ emissions from the fuel exploitation sector are the dominant CH₄ sources in the study area, accounting for 95.5% of the total CH₄ emissions during 2018-2021 (Figure A-2 left). The total estimates originating from the energy sector are around 1.85 × 10²⁷ molec. s⁻¹ (1.6 Tg yr⁻¹). The EDGARv7 estimates a very similar spatial distribution (Figure A-2 right) as the CAMS inventory with slightly higher (4.5%) values in Changzhi. The spatial patterns in Jincheng and Yangquan are presented in Figure A-3.

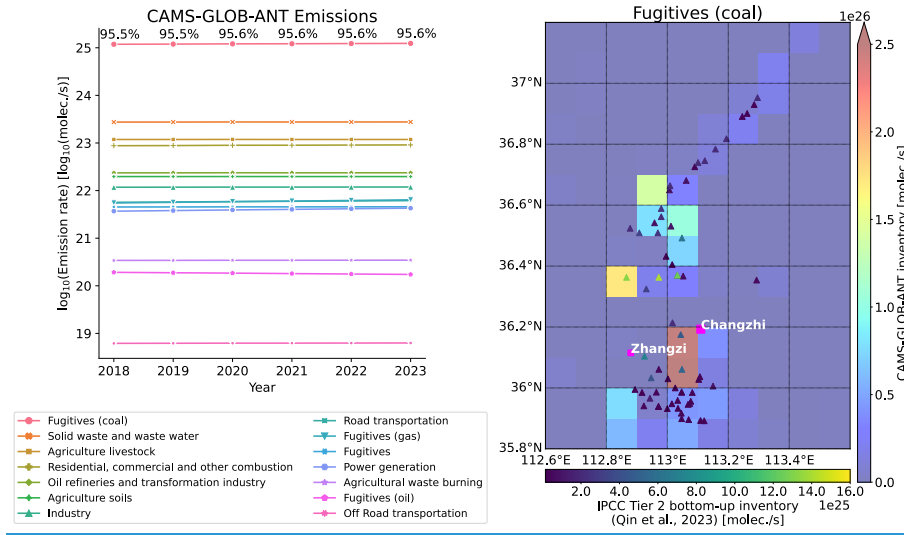


Figure 1: Left: time-series plot of the yearly averaged CAMS global anthropogenic emissions for different sectors for 2018–2023 (<https://permalink.aeris-data.fr/CAMS-GLOB-ANT>, last access: 12 July 2023, Granier et al., 2019). The percentage values represent the share of methane emission from coal production and distribution (fugitives (coal)). Right: spatial distribution of methane emission from coal production for the CAMS-GLOB-ANT inventory. The triangle symbols denote the locations of the coal mines and the respective colors represent their emission rates based on the IPCC Tier 2 bottom-up inventory (Qin et al., 2023).

2.3 Dispersion model

2.3.1 Cone plume model

The CH₄ emerging from a point source is expected to be distributed along the wind direction. It is assumed that the CH₄ molecules disperse evenly along a fan-shaped plume (Tu et al., 2022a). The column enhancement in the downwind side due to the assumed source is represented by the following equation:

$$dcol_{CH_4} = \frac{\varepsilon}{v \cdot d \cdot fov} \quad \text{Eq. (1)}$$

wherein ε represents the emission rate at the source point in molec. s⁻¹, $-v$ is the wind speed in ms⁻¹ [with the ERA5 wind data at 100 m employed in this study](#), d the distance between the source point and the downwind point, and fov the opening angle

of the cone plume in rad. Here f_{ov} is assumed to be 60° based on previous studies (Tu et al., 2022a, b). It should be noted that the point source does not generate enhanced CH_4 concentrations outside of the cone. This may introduce some uncertainties and will be discussed in Sect. 3.4.

150 2.3.2 Gaussian plume model

The dispersion of a gas as a function of distance downwind from a point source can ~~be computed as~~ alternatively be approximated by a Gaussian plume model (Seinfeld and Pandis, 2006). To evaluate the sensitivity of the analysis with respect to the cone plume model assumption, as an alternative a Gaussian plume model is investigated in the following.

$$dcol_{CH_4} = \frac{\varepsilon}{v \cdot d \cdot \sqrt{2\pi} \cdot \left(\frac{f_{ov}}{2}\right)} \cdot \exp\left(-\frac{1}{2} \cdot \left(\frac{\varphi}{\left(\frac{f_{ov}}{2}\right)}\right)^2\right) \quad \text{Eq. (2)}$$

155 where $dcol_{CH_4}$ represents the enhanced column in the downwind direction, the f_{ov} the angle of the opening angle adopted from the cone plume model (Tu et al., 2022a), v the wind direction, d the distance between the point source and the downwind location, and φ the angle of plume axis and the direction under consideration. The $dcol_{CH_4}$ in the cone plume is restricted in the cone area with an opening angle of f_{ov} , while the values in the Gaussian plume show a gradually fading enhancement along the circle arc at any radius d (Figure A- 4). We use the Gaussian plume model here in addition to the cone plume outlined before for enhancing the error estimate of the emissions resulting from our inversions. We estimate the error budget by varying
160 the model parameters of each model description within reasonable limits. Using two alternative models for describing the gas dispersion, in addition enables us to investigate the uncertainties introduced by the chosen model type.

2.4 Background removal and wind-assigned anomaly method

It is of importance to separate the increase of the atmospheric CH_4 concentration due to local emissions from the accumulated atmospheric CH_4 background concentration (the CH_4 atmospheric lifetime is in the order of 12 years). A Jacobian matrix is
165 introduced to reconstruct the background according to a few background model coefficients, i.e., a constant CH_4 value and ~~r~~ superimposed disturbances: a temporal linear increase, a seasonal cycle determined by the amplitude and phase of the three frequencies 1/year, 2/year and 3/year, a daily signal (same value for all data measured during a single day), and a horizontal gradient (same value for any time but dependent on the horizontal location) (Tu et al., 2022a). In the following discussion, the satellite enhancements refer to the residual signal as deduced from TROPOMI CH_4 observations after subtracting the modelled
170 background (Figure 4 lower panel).

The wind-assigned anomaly method was first developed ~~in~~ for quantifying CH_4 emissions from landfills in Madrid (Tu et al., 2022a). Its applicability for estimating the CMM emissions in the Upper Silesian Coal Basin (USCB) in southern Poland was demonstrated afterwards (Tu et al., 2022b). The wind-assigned anomalies refer to the difference of enhancements under two opposite wind regimes ((e.g., NW ($>215^\circ$ and $<45^\circ$) and SE ($45^\circ - 215^\circ$) fields for Changzhi region). The wind regimes
175 are divided mainly based on the predominant wind fields over the study regions. The expected daily enhancements (plumes)

generated by individual emission sources are computed based on Eq. (1) and all contributions then are superimposed to obtain a total daily pattern of CH₄ enhancement due to local sources. A temporally averaged pattern is obtained for each wind regime over the study period and the difference between the two patterns is therefore the modeled wind-assigned anomaly. The empirical anomalies are computed from the satellite XCH₄ data. The estimated emission rate is computed by scaling the modeled anomalies to the empirical anomalies. The uncertainties of the empirical anomalies are determined by the deficits of the background model resulting in an imperfect elimination of the background, and the noise errors in the satellite observations.

3. Results and discussion

3.1 TROPOMI observations

Shanxi province is rich in coal resources, and as a result, there are more than 600 coal mines spread across the province. Most of these coal mines are concentrated in the northern, eastern and southeastern, and central regions of China Shanxi. A multi-year average of TROPOMI XCH₄ observations in the whole Shanxi province is shown in Figure 2, superimposed to the locations of mines in the area. Elevated XCH₄ is observed in three regions: Yangquan (east), Changzhi (southeast) and Jincheng (south). Of these regions, the Changzhi region is of particular interest since a field campaign was implemented in 2022. This field campaign region covers an area of 35.8°N–37.2°N, 112.6°E–113.6°E, i.e., 155 km × 90 km) and will be discussed in detail as an example to better understand the CH₄ emissions from coal mining activities in Shanxi province.

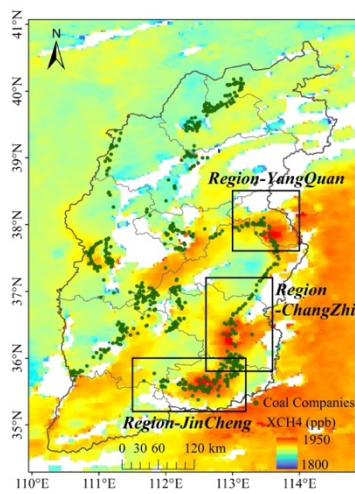
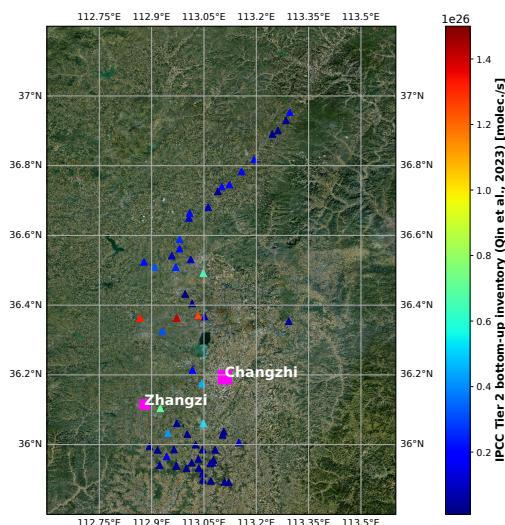


Figure 2: TROPOMI XCH₄ and the location of coal mines in Shanxi province. Green dot symbols denote the coal mine locations (<http://nyj.shanxi.gov.cn/>, last access: August 21, 2023).

There are 62 coal mines located over the study area in Changzhi region, as shown in Figure 3. The emission rates range from 1.6×10^{24} to 1.4×10^{26} molec. s⁻¹ (~ 0.001 Tg yr⁻¹ – 0.11 Tg yr⁻¹) (Qin et al., 2023). There are near 30 small coal mines scattered in the mountain area in the south and each mine has a relatively low emission rate, measuring less than 1.0×10^{25}

molec. s⁻¹ the emissions are relatively small with 24 orders of magnitude in molec. s⁻¹. Some larger coal mines with higher emissions rates (emission rate > 1.0×10^{25} molec. s⁻¹) are found close to the Zhangzi county as well as in the north region and the mean value for these is around 7.3×10^{25} molec. s⁻¹ with a standard deviation of 4.6×10^{25} molec. s⁻¹.



200

Figure 3: Terrain map with IPCC Tier 2 bottom-up inventory (Qin et al., 2023). The triangle symbols represent the location of all individual coal mines, and different colors denote the emission rates. The square symbols denote the locations of Changzhi city and Zhangzi county. Terrain information originates from World Imagery.

A time series of five-years of TROPOMI XCH₄ observations in the Changzhi region is shown in Figure 4. The average concentration is 1906.8 ± 41.0 ppb over the entire period. From 2019 to 2022, there is an observed increase in XCH₄ levels by approximately 0.7% per year. The observations in the figure indicate that there is a clear seasonal variability in the concentrations. The data shows that the lowest abundances of XCH₄ occur in the early part of the year, while the highest values are observed in autumn. The seasonal pattern is determined by both sinks and sources. The elimination of methane (CH₄) by hydroxyl radicals (OH) in the troposphere, known as atmospheric oxidation, plays a crucial role in controlling the concentrations of climate-relevant gases like CH₄ (Rigby et al., 2017; Li et al., 2018). This process is responsible for approximately 85-90% of atmospheric CH₄ loss (Saunois et al., 2020). On the other hand, the dominant factor contributing to CH₄ emissions in this region is coal mining activities. These coal production activities can vary throughout the year and have a significant impact on the overall XCH₄ concentrations.

210

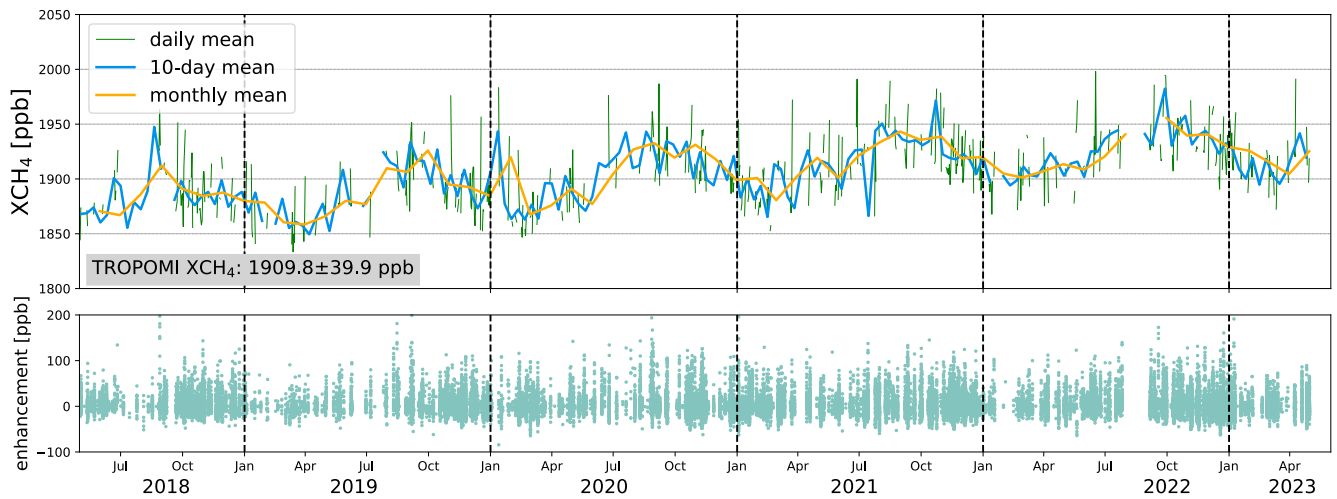


Figure 4: Time-series of average TROPOMI XCH₄ (upper panel) and corresponding enhancement after removing the background (lower panel) over Changzhi region (35.8°N—37.2°N, 112.6°E—113.6°E) from May 2018 to April 2023.

3.2 CH₄ inventories

The yearly-mean of CAMS GLOB-ANT for 14 sectors are illustrated in Figure 4a. Emissions from maritime transport in the study area are zero and not shown here. The inventory very well presents the dominant emission sources in the study area. The coal production (fugitives (coal)) is the dominant source of methane emissions, accounting for 96% in total emissions. The sector of solid waste and waste water is the secondary emission source which drops to 2%. Figure 4b shows the spatial distribution of coal emission. The locations of the coal mines and the corresponding emission rates fit well with the CAMS inventory. About half of the coal mines are concentrated in the southern region, while the other half are located further north, along a southwest to northeast direction. The two reddish grids (36.05°N–36.15°N, 113.05°E) denote the highest emission rate in the CAMS inventory, partly due to the Changzhi city, which is located nearby. The CH₄ emission in the city region are primarily attributed to the traffic (particularly during the morning and evening rush hours), CH₄ leaks at gas stations and the utilization and release of natural gas in residential areas (Liu et al., 2022). The CH₄ emission accounts for 1.77×10^{27} molec. s⁻¹ (1.5 Tg yr^{-1}) for the whole study area, which is 55% higher than the bottom-up inventory (1.14×10^{27} molec. s⁻¹— 0.96 Tg yr^{-1}).

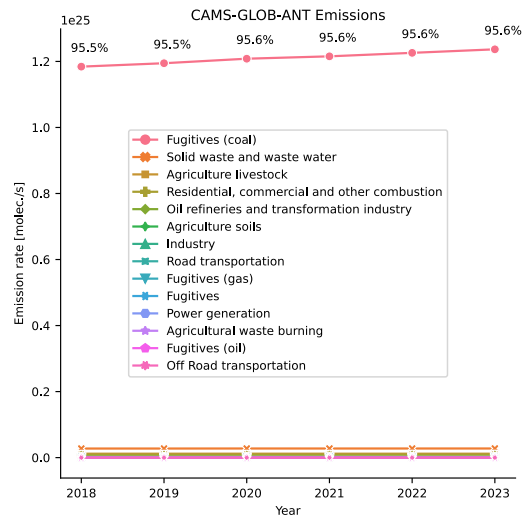


Figure 4: Left: time-series plot of the yearly averaged CAMS global anthropogenic emissions for different sectors for 2018–2023 (<https://permalink.aeris-data.fr/CAMS-GLOB-ANT>, last access: 12 July 2023, Granier et al., 2019). The percentage values represent the share of methane emission from coal production and distribution (fugitives (coal)). Right: spatial distribution of methane emission from coal production for the CAMS-GLOB-ANT inventory. The triangle symbols denote the locations of the coal mines and the respective colors represent their emission rates based on the bottom-up inventory (Qin et al., 2023).

The CH₄ emissions from the fuel exploitation sector are the dominant sources in the study area, which accounts for 95.5% from 2018–2021. The total estimates originating from the energy sector are around 1.85×10^{27} molec. s⁻¹ (1.6 Tg yr⁻¹). The EDGARv7 estimates present a very similar spatial distribution (Figure A–1) as the CAMS inventory with slightly higher (4.5%) values.

3.2 Estimation of CH₄ emission strengths from TROPOMI data sets

The ERA5 wind at 100 m altitude above ground is used for describing the transport ~~for~~ with the wind-assigned method. The wind is segmented as NW (>215° and <45°) and SE (45° – 215°) fields for Changzhi region (Figure A–5). Due to the observed seasonal changes in XCH₄, the observed variable background concentrations need to be considered when estimating the emissions. The TROPOMI enhancements after removing the background are shown in Figure 5a. High values are observed in the center and south of the study area, i.e., close to the clusters of the coal mines (triangle symbols). It is difficult to distinguish the CH₄ from the residential regions since the coal mines are located close to Zhangzi county and Changzhi city. The averaged enhancements are 4.7 ppb ± 5.6 ppb for the whole region. The wind-assigned anomalies from the TROPOMI observations indicate the difference of the enhancements for wind coming from NW and from SE, resulting in a positive plume in the SE direction and negative plume in NW direction (Figure 5b).

The correlation of the wind-assigned anomalies deduced from the TROPOMI observations and from the plume model using the IPCC Tier 2 bottom-up inventory (Qin et al., 2023) is presented in Figure 5c, and the estimated emission rate is $8.4 \times 10^{26} \pm 1.6 \times 10^{25}$ molec. s⁻¹ (R² = 0.61). [In comparison to our results based on the TROPOMI observations and the wind-assigned](#)

method. The IPCC Tier 2 bottom-up (Qin et al., 2023), CAMS and EDGARv7 inventories are overestimating the emissions, and have a high bias by with 31%, 120% and 130% higher than the estimate based on the TROPOMI observations and the wind-assigned method, respectively.

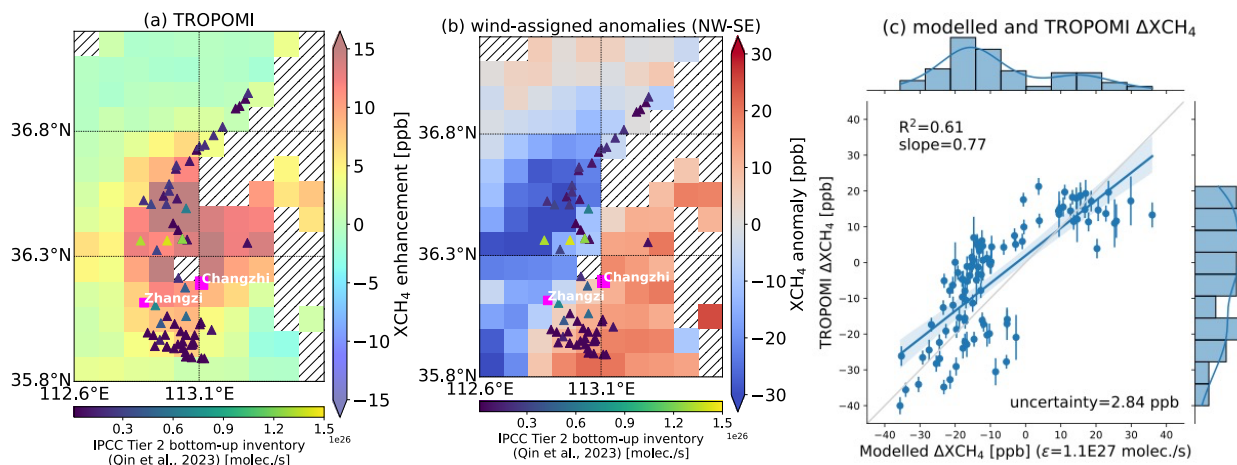
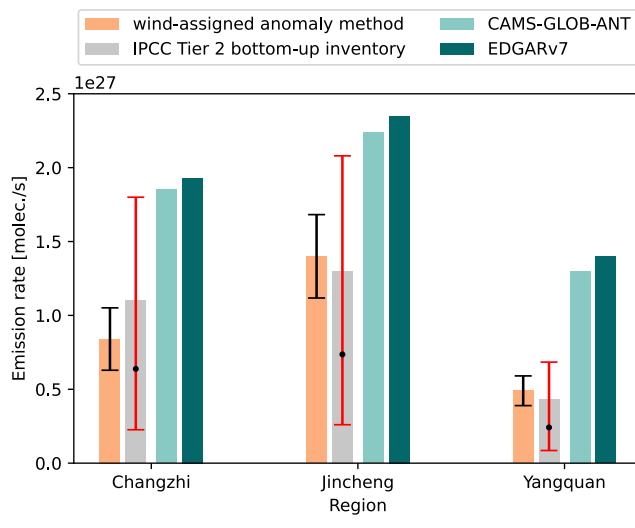


Figure 5: TROPOMI XCH₄ enhancement (XCH₄-background) (a), the wind-assigned anomalies (NW-SE) (b), and correlation plot of the wind-assigned anomalies (c) between TROPOMI and the simple cone plume model with using the IPCC Tier 2 bottom-up inventory (1.1×10^{27} molec. s⁻¹ in total, Qin et al., 2023) and ERA5 wind at 100 m during May 2018–May 2023 over the Changzhi region. The triangle symbols denote the inventory locations, with different colours indicating varying emission rates. Hatched areas in (a)–(b) indicate grids with no available data. The uncertainty in (c) is presented by the average error bars of the anomalies, which are derived from the uncertainty in the background and the TROPOMI observations.

The wind-assigned method was also applied to Jincheng and Yangquan regions. The wind segmentations are NW-SE for Jincheng and E-W for Yangquan based on the ERA5 wind information (Figure A-5). The estimated emission is $1.4 \times 10^{27} \pm 1.9 \times 10^{25}$ molec. s⁻¹ for Jincheng and $4.9 \times 10^{26} \pm 1.8 \times 10^{25}$ molec. s⁻¹ for Yangquan. The wind-assigned anomalies in the Jincheng region shows a better correlation with a R² value of 0.80, whereas the value is lower (R²=0.42) in the Yangquan region (Figure A-6). The resulting estimate for Jincheng is close to the IPCC Tier 2 bottom-up inventory (Qin et al., 2023), displaying a minor deviation of around 8%. However, the distinction is more pronounced for Yangquan, exhibiting a slightly larger difference of 14%. Figure 6 summarizes the estimated emissions based on the wind-assigned anomaly method compared to the predictions based on the inventories in all regions. In general, the estimates are comparable to the IPCC Tier 2 bottom-up inventory (Qin et al., 2023), whereas both CAMS and EDGAR inventories overestimate the emissions with a relative difference of about 120%/130% in Changzhi, 60%/68% in Jincheng and 165%/186% in Yangquan.

Our CMM estimates in these three regions fall within the 30th and 70th percentile range of the updated emission rates in the study by Qin et al. (2023). In addition, our results are consistently lower than the CAMS-GLOB-ANT and the EDGARv7 inventories. This result agrees with previous studies. For instance, a -15% underestimation compared to the UNFCCC has been reported by Chen et al., (2022). Additionally, Zhang et al., (2021) documented a 30% decrease in their posterior estimates for China, with 60% attributed to coal mining. This pattern of overestimated anthropogenic emissions, in comparison to China's inventory, has also been found in previous research, utilizing GOSAT inversion and various versions of the EDGAR inventory

280 as a priori estimates (Miller et al., 2019; Maasackers et al., 2019). This divergence may be attributed to two reasons: (1) missing
observation of strong CMM emissions during the TROPOMI overpass. It is important to note that CMM emissions exhibit a
strong dependency on coal mine activities, which vary over time. The TROPOMI data provide instantaneous observations,
capturing CH₄ concentrations at a specific moment (local time ~ 13:30), thereby leading to limitations in detecting strong
CMM emissions during both morning and afternoon periods. (2) the CMM utilization connected with a reduction of release
285 into the atmosphere has been largely improved in the last decade, since the national government issued specific targets in the
national 12th and 13th five-year plan (Gao et al., 2021; Lu et al., 2021).



290 **Figure 6: Estimated emission rates and emission rates from three different inventories for the Changzhi, Jincheng and Yangquan regions. The dot symbols in the grey bars represent the emission rates updated with the flux tower observations with 50th percentile of distribution, and the bottom and top error bars (red) represent the values with 30th and 70th percentile, respectively (Qin et al., 2023).**

3.3 Uncertainty analysis

3.3.1 Background removal

295 In comparison to the atmospheric concentration, the CH₄ amounts emitted from the sources are relatively small (Figure 4).
To assess the impact of background removal sensitivity, the 10th lower percentile of overall satellite observations each day is
considered as the background for the study area on that day, instead of separately considering the spatial and temporal variation
as described in Section 2.3. The XCH₄ enhancements using the new background removal method, are generally higher than
those achieved with the previous approach, exhibiting a mean bias of 21.5 ± 14.4 ppb in Changzhi (Figure A- 7a). This
discrepancy diminishes to -3.6 ± 2.1 ppb when comparing the wind-assigned anomalies computed from TROPOMI
300 enhancements based on different background removal methods (Figure A- 7b). Calculating the differences in enhancements
under two different wind field segmentations helps to reduce systematic errors associated with the background removal. The

substitution of the background removal method results in a 7% increase in estimated emission rates in Changzhi, a 6% increase in Jincheng and a 9% increase in Yangquan.

3.3.2 Cone plume and Gaussian plume model

305 The wind assigned method uses the cone plume model, in which the emitted molecules are dispersed evenly within a cone shape area (Tu et al., 2022a, b). To evaluate the sensitivity of the analysis with respect to the assumption, an alternative Gaussian plume is investigated in the following.

$$dcol_{CH_4} = \frac{\epsilon}{v \cdot d \cdot \sqrt{2\pi} \cdot \left(\frac{fov}{2}\right)} \cdot \exp\left(-\frac{1}{2} \cdot \left(\frac{\varphi}{\left(\frac{fov}{2}\right)}\right)^2\right) \quad \text{Eq. (2)}$$

310 where $dcol_{CH_4}$ represents the enhanced column in the downwind direction, the fov the angle of the opening angle adopted from the cone plume model (Tu et al., 2022a), v the wind direction, d the distance between the point source and the downwind location, and φ the angle of plume axis and the direction under consideration. The $dcol_{CH_4}$ in the cone plume is restricted in the cone area with an opening angle of fov, while the values in the Gaussian plume show a gradually fading enhancement along the circle are at any radius d (Figure A-6).

To further investigate the uncertainty of the two plume models, different opening angles are tested for estimating CH₄ emissions in the [study Changzhi regions](#). Estimated emissions increased with increasing fov for both plume models [\(Figure 7 for Changzhi, and Figure A- 8 for Jincheng and Yangquan\)](#). The results based on the Gaussian plume is higher than those based on the cone plume and the discrepancy between the two models increases with increasing opening angle. [For Changzhi region](#), [When the fov is chosen as the previous setting value \(60°\)](#), the estimated emission rate based on the Gaussian plume are $9.4 \times 10^{26} \pm 1.7 \times 10^{25} \text{ molec. s}^{-1}$, which is 12% higher that based on the cone plume model. The relative difference between these two models drops to 5% for $fov = 20^\circ$. The anomalies derived from the Gaussian plume model [are](#) overall similar to those from the cone plume model, showing a slightly better correlation with the anomalies from the TROPOMI observations ($R^2 = 0.65$, [Figure A- 9](#)).

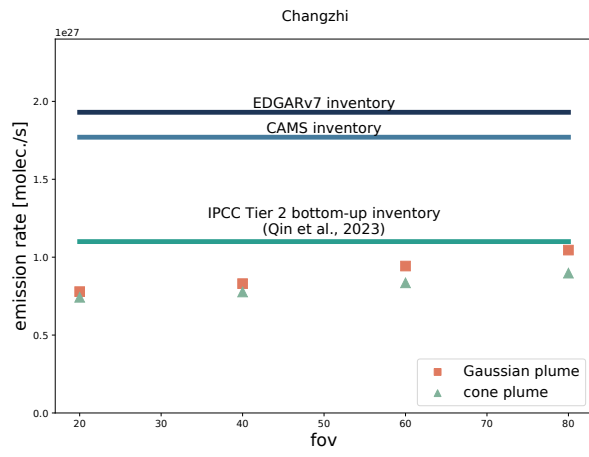


Figure 7: Estimates of emission rates in Changzhi region with respect to different opening angles based on cone plume and Gaussian plume model. The three different inventories are presented as well.

325 3.3.3 Wind analysis data and field segmentation

Uncertainty in wind direction and speed is one of the largest sources of error in correctly estimating the emission rates (Tu et al., 2022b). Thus, use of winds at different model height level and different wind field segmentations are tested, the spatial variation of the winds is investigated, and an alternative~~other~~ wind data set is applied ~~associated with~~ for the wind-assigned ~~method are investigated~~ anomaly analysis.

330 The wind direction exhibits a similar pattern at 10 m and 100 m model levels, while the speed increases with height. The wind speed at 10 m is 15.4% lower than that at 100 m in Changzhi region. Consequently, the corresponding estimated emission rate amounts to 7.4×10^{26} molec. s^{-1} , representing an 11.9% decrease compared to the estimate obtained using wind data at 100 m. Using 10 m winds instead of 100 m reduces the emission estimates by 10.7% (the average wind speed reduces by 17%) in Jincheng and 4.1% (the average wind speed reduces by 10%) in Yangquan for wind at 10 m, in comparison to those using
335 wind data at 100 m. The wind segmentation is mainly based on the local predominant wind regimes. To quantify its uncertainty, different segmentations (N and S segmentations for Changzhi and Jincheng, and NW and SE segmentations for Yangquan) are applied. The corresponding CH₄ emission increases by 12% in Changzhi, whereas it decreases by 7% in Jincheng and by 6% in Yangquan.

The topography can affect the surface wind, making it challenging to determine the exact pathway of transport from the
340 emission source to the measurement station (Babenhauserheide et al., 2020). Considering the elevation features, the central part of the Changzhi region is characterized by flat terrain, while elevations rise in the northeast and southeast, as depicted in Figure A- 10. To further investigate the sensitivity of the wind spatial variation, the wind data at the central point (36.5° N, 113° E for Changzhi, 35.5° N, 112.75° E for Jincheng and 38° N, 113.5° E in Yangquan) is used as a representative value to represent the wind for the entire study area. The wind direction pattern at the central point tends to have more wind from east
345 and the averaged wind speed decreases only by 4.4% compared to that over the whole study area in Changzhi (Figure A- 11). This substitution results in a decreased estimated emission rate with 11% (emission rate: 7.5×10^{26} molec. s^{-1}) in Changzhi, an increased emission rate with 7% (1.5×10^{27} molec. s^{-1}) in Jincheng and 8% (5.3×10^{26} molec. s^{-1}) in Yangquan.

An alternative wind dataset at a height of 100 m above the ground from the Global Data Assimilation System (GDAS) are used instead of the ERA5 dataset. The GDAS ~~provides the National Centers for Environmental Prediction (NCEP)-FNL (Final~~
350 operational global analysis and forecast data is provided by the National Centers for Environmental Prediction (NCEP) with a spatial resolution of $0.25^\circ \times 0.25^\circ$ and a temporal resolution of 6 h (National Centers for Environmental Prediction et al., 2015). Compared with the ERA5 data, the NCEP data shows comparable wind distributions (Figure A- 13), featuring slightly elevated wind speeds and a more prevalent wind direction originating from the broader northwest region. The estimated emission strength for using the NCEP dataset amounts to $7.9 \times 10^{26} \pm 1.6 \times 10^{25}$ -molec. s^{-1} , indicating a 6% reduction compared to the

355 value obtained using the ERA5 dataset [in Changzhi](#). [The estimates increase by 7% in Jincheng and decrease by 2% in Yangquan.](#)

3.3.4 Inventories

The use of an inventory as a priori knowledge is integral to the wind-assigned anomaly approach. As detailed in Sect. 3.2, the [IPCC Tier 2](#) bottom-up and the CAMS-GLOB-ANT (or EDGAR) inventories highlight discrepancies in emission sources both in terms of location and abundance. To investigate the uncertainty introduced by the inventory, the CAMS-GLOB-ANT inventory is employed in the approach instead of the [IPCC Tier 2](#) bottom-up inventory. Given the similarity in pattern between the CAMS and EDGAR inventories, we have exclusively focused on the CAMS inventory. This substitution leads to minor deviations in the [observed](#) enhancements ([TROPOMI XCH₄](#) - background) across the Changzhi region (Figure A- 14(a) and Figure 5(a)). In general, the spatial patterns maintain a notable similarity, while presenting some divergence in abundance. The calculated average stands at 3.61 ± 4.44 ppb when employing the CAMS-GLOB-ANT inventory. In contrast, using the [IPCC Tier 2](#) bottom-up inventory yields an average of 4.68 ± 5.59 ppb. [These two datasets show a mean bias of \$1.12 \(\pm 2.93\)\$ ppb with an \$R^2\$ value of 0.8562](#) (Figure A- 14(b)). The wind-assigned anomalies from both datasets also present comparable patterns and display a strong correlation between them ([Figure A- 14\(c\)](#), $R^2 = 0.9962$). It is because the systematic errors in background removal is compensated by computing the differences of enhancements under different wind field segmentations. The estimated emission strength amounts to $8.5 \times 10^{27} - 10^{26} = 1.8 \times 10^{25}$ molec. s⁻¹ [in Changzhi, which is very close \(1%\) to the strength estimated using the Tier 2 IPCC bottom-up inventory as the a priori. Similar results are observed in the other two regions, with biases of 7% higher and 12% lower biases in Jincheng and Yangquan, respectively.](#)

[Based on the error propagation, the total uncertainties in the estimated emission rates from the different error sources \(background removal and noise in the satellite data, dispersion model \(Gaussian plume and opening angle \$fov = 70^\circ\$ \), wind information \(ERA5 wind for height level = 10 m, wind without considering spatial variation, different wind segmentation, and NCEP wind data\), and different inventories\) are approximately 25% for Changzhi, 20% for Jincheng and 21% for Yangquan.](#)

4. Conclusion

Quantifying CMM emissions using high-spatial resolution satellite observations can contribute independent emission estimates for evaluating inventories and assisting in the development of reduction strategies and interventions. In this study, a wind-assigned anomaly method was used for analyzing the TROPOMI XCH₄ observations between May 2018 to May 2023. The CMM emissions in three subregions (Changzhi, Jincheng, Yangquan) in the coal-rich Shanxi province of China were ~~achived~~ [achieved](#). The three regions are aggregation areas of coal mines, consequently exhibiting elevated XCH₄ abundances. The concluded emission strengths are $8.4 \times 10^{26} \pm 1.6 \times 10^{25}$ molec. s⁻¹ (0.706 ± 0.013 Tg yr⁻¹, $\pm 25\%$), $1.4 \times 10^{27} \pm 1.9 \times 10^{25}$ molec. s⁻¹ (1.176 ± 0.016 Tg yr⁻¹, $\pm 20\%$), and $4.9 \times 10^{26} \pm 1.8 \times 10^{25}$ molec. s⁻¹ (0.412 ± 0.015 Tg yr⁻¹, $\pm 21\%$), respectively.

385 ~~When comparing the estimates with three different inventories (bottom-up, CAMS-GLOB-ANT, and EDGARv7.0),~~ The
estimates obtained ~~using derived through~~ the wind-assigned anomaly method ~~are demonstrate comparability with comparable~~
~~to the bottom-up~~ the IPCC Tier 2 bottom-up inventory (Qin et al., 2023). Compared to the estimates, the inventory shows
~~inventories, relative with relative~~ differences of 31%, -7%, and -12% in Changzhi, Jincheng, and Yangquan, respectively. Our
390 CMM estimates in these three regions fall within the 30th and 70th percentile range of the updated emission rates in the study
by Qin et al. (2023). The CAMS-GLOB-ANT and EDGARv7.0 inventories show very similar results. However, higher
discrepancies are found when comparing our estimates to these inventories, with differences reaching approximately 125%,
64%, and 176%, respectively. This indicates a potential overestimation of CH₄ emissions from these coal mining regions in
the CAMS-GLOB-ANT and EDGARv7.0 inventories. Previous studies have also documented similar trends, reporting
395 overestimated CMM emission estimates in inventories (Chen et al., 2022; Zhang et al., 2021; Miller et al., 2019; Maasackers
et al., 2019). In addition, our lower estimates might due to two reasons: (1) a lack of observation of strong CMM emissions
during TROPOMI overpasses. CMM emissions are closely tied to coal mine activities, which exhibit temporal variability.
TROPOMI data provide instantaneous observations, capturing CH₄ concentrations at a specific local time (~ 13:30), which
may limit the detection of strong CMM emissions during morning and afternoon periods. (2) improvement in CMM and
400 reduction of atmospheric release have been substantial in the last decade. This improvement is attributed to specific targets set
by the national government in the national 12th and 13th five-year plan (Gao et al., 2021; Lu et al., 2021), indicating a potential
decrease in actual emissions compared to historical inventory estimates.

To evaluate uncertainties, we explore variations in background removal, the dispersion model and its inputs (wind data and
inventory serving as a priori knowledge). The background removal introduces upward biases in 6%-9% when using the 10th
405 lower percentile of overall satellite observations each day as the background for the study area on that day. The cone plume
model introduces uncertainties due to assuming a sharply ~~boarded-bordered~~ fan-shaped plume extending along the downwind
direction, i.e., any points located outside of the cone area experience no enhancement. To estimate ~~the~~ uncertainties connected
to the assumed plume shape, we investigate the assumption of a Gaussian plume, resulting in an estimated emission strength
increase of 12%, 7% and 8% in Changzhi, Jincheng, and Yangquan, respectively. Beyond ~~the~~ consideration of the dispersion
model, the assumed wind speed and direction represent is a major sources of uncertainty. An analysis of using wind at 10 m
410 height reveals lower biases of 4%-12%. Additionally, we tested an alternative wind category (N-S), yielding a 10% increase
in estimated emission strength in Changzhi and 7% and 6% decrease in Jincheng and Yangquan (NW-SW), respectively.
Considering the elevation features, the spatial variation in wind leads to median biases ranging from 6% to 9%. a Introducing
another wind dataset (NCEP FNL) for analysis results in different biases of -6%, 7% and -2% in the three different regions.
~~Additionally, we tested an alternative wind category (N-S), yielding a 12% increase in estimated emission strength.~~ The
415 emission inventory is considered as a priori knowledge in the approach and replacing the IPCC Tier 2 bottom-up inventory
with the CAMS-GLOB-ANT inventory introduces ~~a very~~ small biases of (1%, 7% and -12%). Considering all the impacts
mentioned above, the total uncertainties, computed through error propagation, are determined to be 25% in Changzhi, 20% in
Jincheng and 21% in Yangquan.

420 This study further demonstrates the practicality of employing the wind-assigned anomaly method together with the high spatial resolution TROPOMI XCH₄ to quantify regional-scale CH₄ emission strengths. This approach holds promise for extending its application to estimate CMM emission in other coal mine-active regions, thereby providing top-down estimates that can enhance the refinement of inventories. Moreover, these results offer support for enhancement of the mitigation strategies and the efficient control of CMM emissions.

425

Data availability. The TROPOMI data set is publicly available from <https://scihub.copernicus.eu/> (last access: 29 July 2023; ESA, 2020). The access and use of any Copernicus Sentinel data available through the Copernicus Open Access Hub are governed by the legal notice on the use of Copernicus Sentinel Data and Service Information, which is given here: 430 https://sentinels.copernicus.eu/documents/247904/690755/Sentinel_Data_Legal_Notice (last access: 29 July 2023; European Commission, 2020).

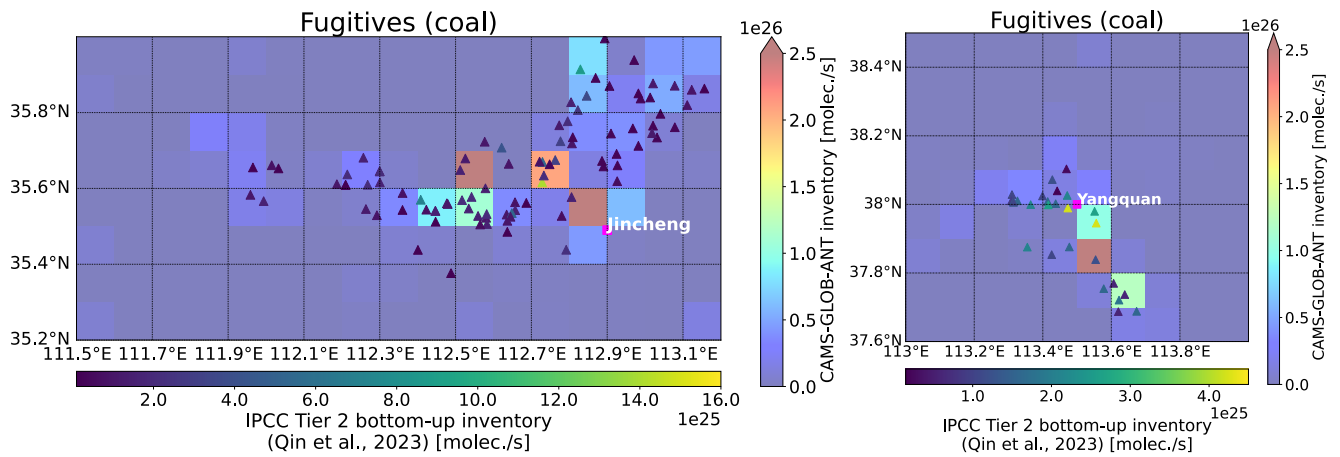
Author contributions. QT and FH developed the research question. QT wrote the manuscript and performed the data analysis with input from FH. QK and JC supplied the [IPCC Tier 2](#) bottom-up inventory and local insights for the study regions. XZ 435 designed and created parts of the graphics. FK and QK participated in result discussions and contributed to improve the paper. All authors contributed to the interpretation of the results and the improvement of the manuscript.

Competing interests. At least one of the (co-)authors is a member of the editorial board of Atmospheric Chemistry and Physics.

440 *Acknowledgements.* We would like to thank Emissions of atmospheric Compounds and Compilation of Ancillary Data (ECCAD) for providing CAMS-GLOB-ANT inventory data and the Emissions Database for Global Atmospheric Research (EDGAR) for providing EDGARv7.0 inventory data. Thanks should also go to the TROPOMI team for making CH₄ data publicly available.

445 *Financial support.* This study was supported by the National Natural Science Foundation of China (grant no. 42305138), the Shanxi Province Major Science and Technique Program (grant no. 202101090301013) and the Fundamental Research Funds for the Central Universities.

Appendix



450

Figure A- 1: Similar to Figure 1-right, but for Jincheng (left) and Yangquan (right) regions, respectively.

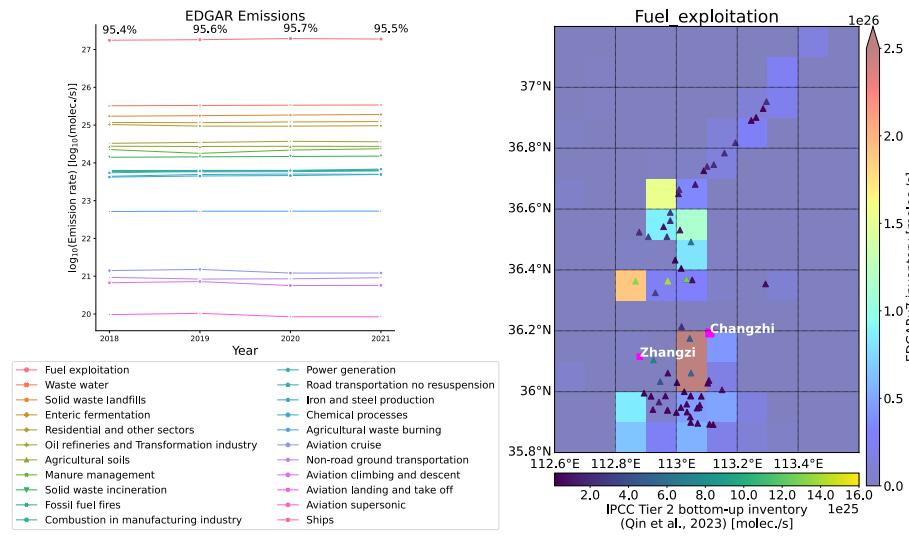
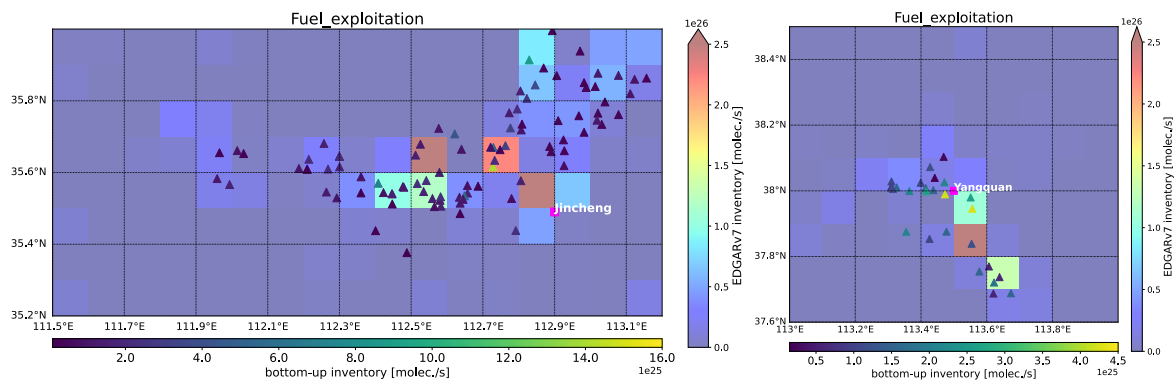


Figure A- 2: Similar to Figure 1 but for the EDGARv7 energy sector in Changzhi.



455 **Figure A- 3:** Similar to Figure 1-right, but for the EDGARv7 energy sector in Jincheng (left) and Yangquan (right) regions, respectively.

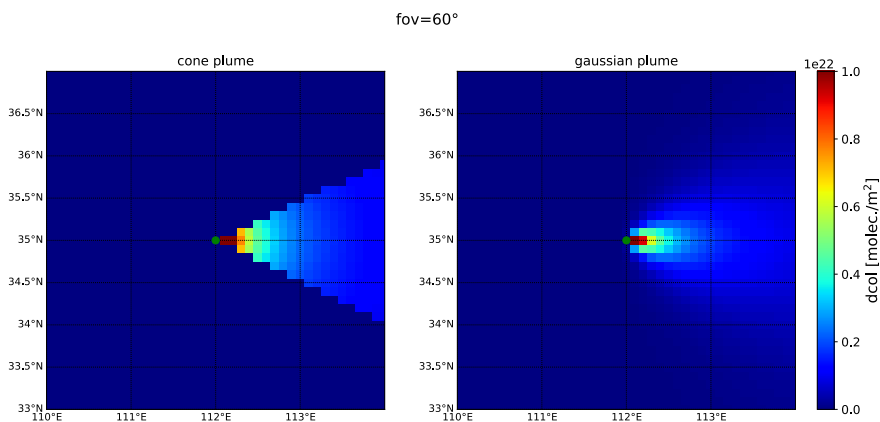


Figure A- 4: Spatial distribution of dispersion based on the cone plume (left) and Gaussian plume (right) model. The wind from west is used as an example.

460

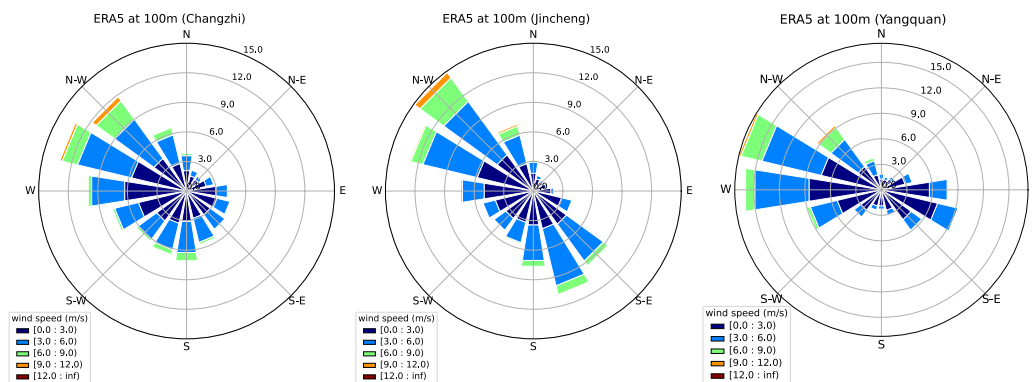
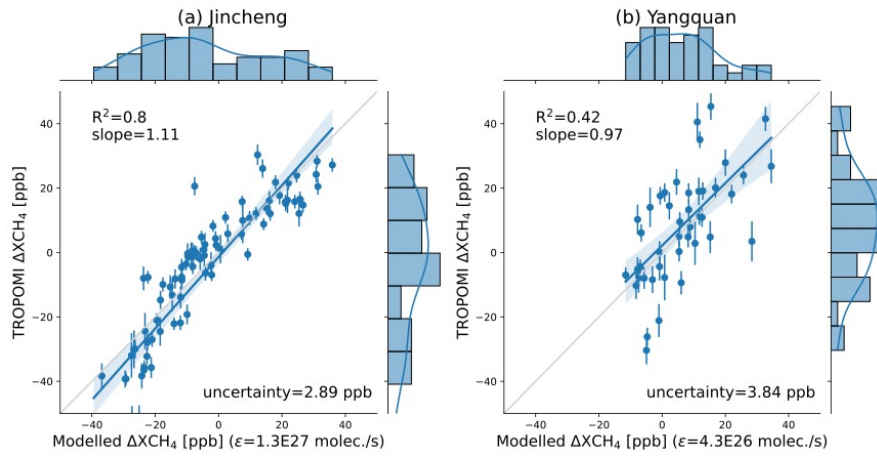


Figure A- 5: Wind roses plots for local daytime (08:00–18:00 UTC) from May 2018 to April 2023 for the ERA5 model wind in Changzhi, Jincheng and Yangquan regions, respectively.



465

Figure A- 6: Similar to Figure 5(c), but for the Jincheng and Yangquan regions.

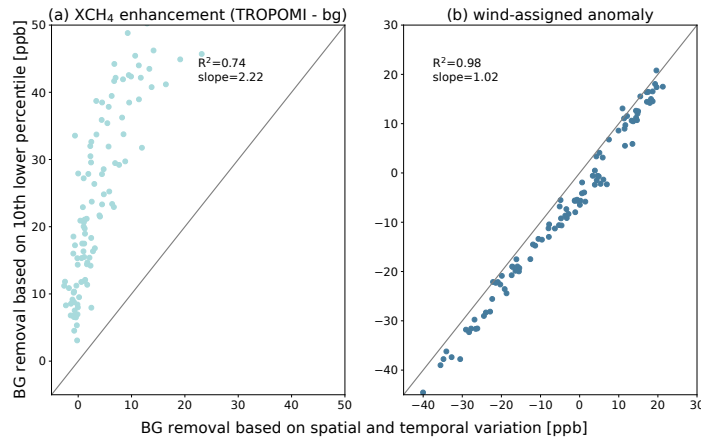
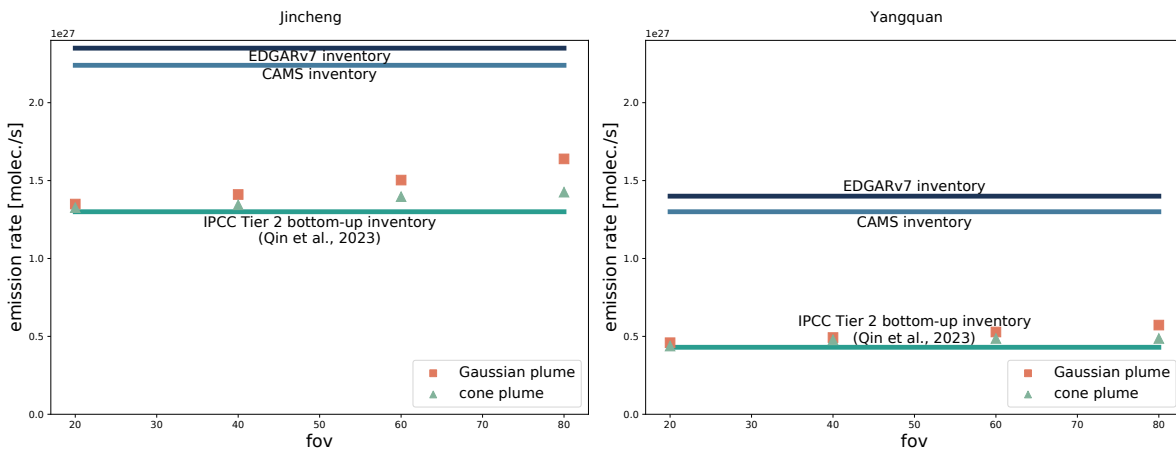


Figure A- 7: XCH₄ enhancements (TROPOMI - background) and its corresponding wind-assigned anomaly using different background removal methods. The grey solid line corresponds to the 1:1 line.



470

Figure A- 8: Similar to Figure 7 but for Jincheng and Yangquan regions.

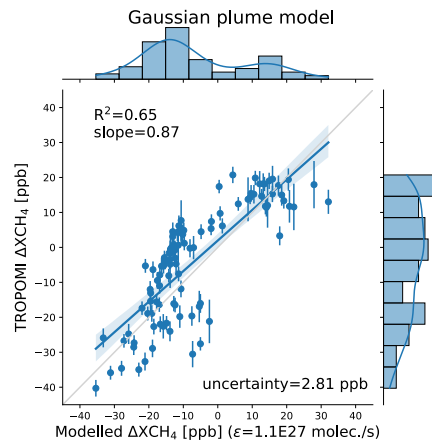


Figure A- 9: Similar to [Figure 5](#) [Figure 5\(c\)](#) but using the Gaussian plume model.

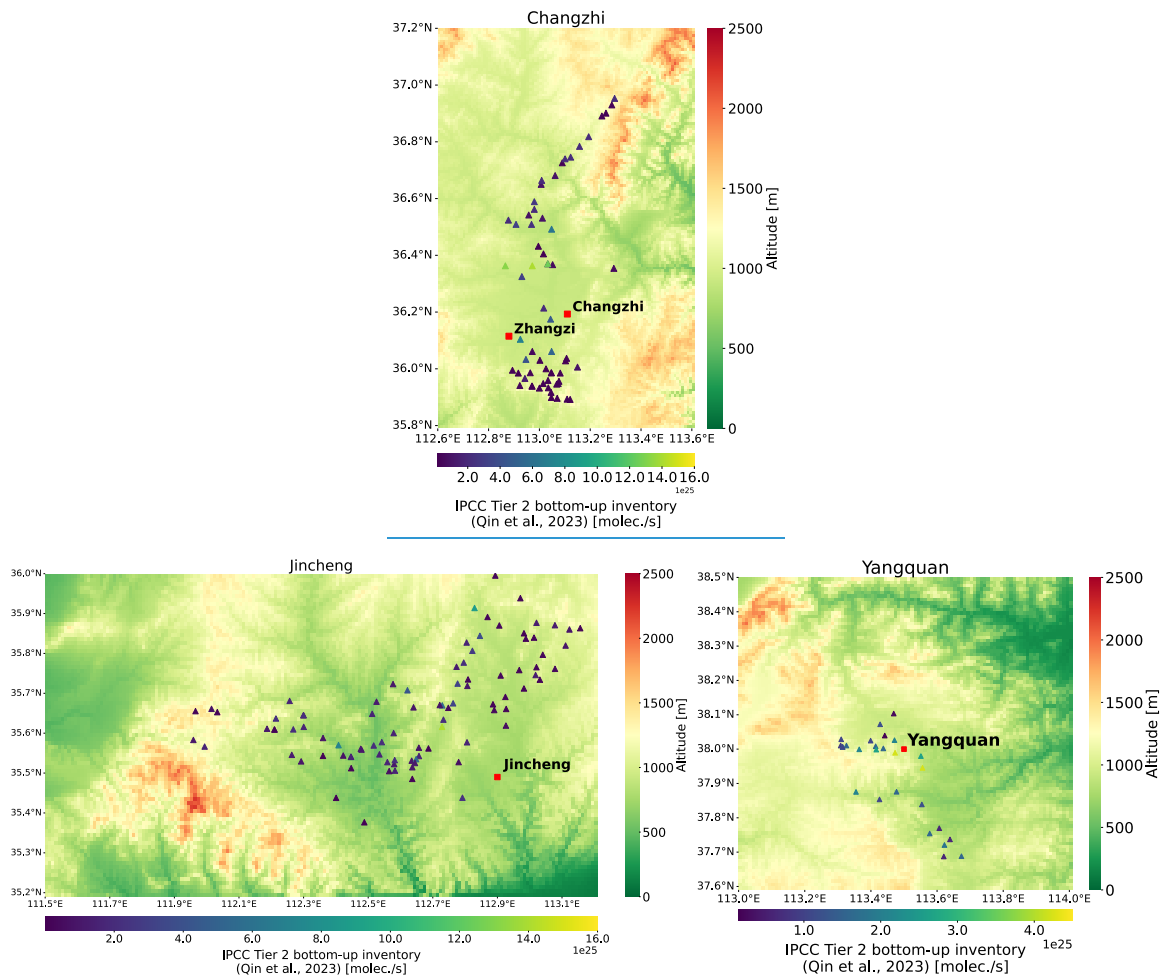


Figure A- 10: Altitude map for Changzhi, Jincheng and Yangquan regions. Data originate from ALOS World 3D – 30m (AW3D30) ([Tadono et al., 2014](#)).

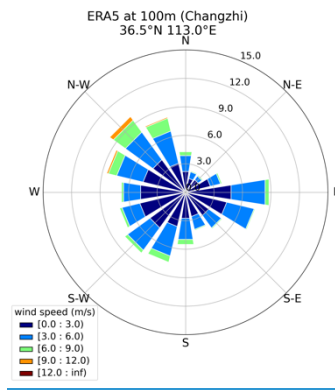
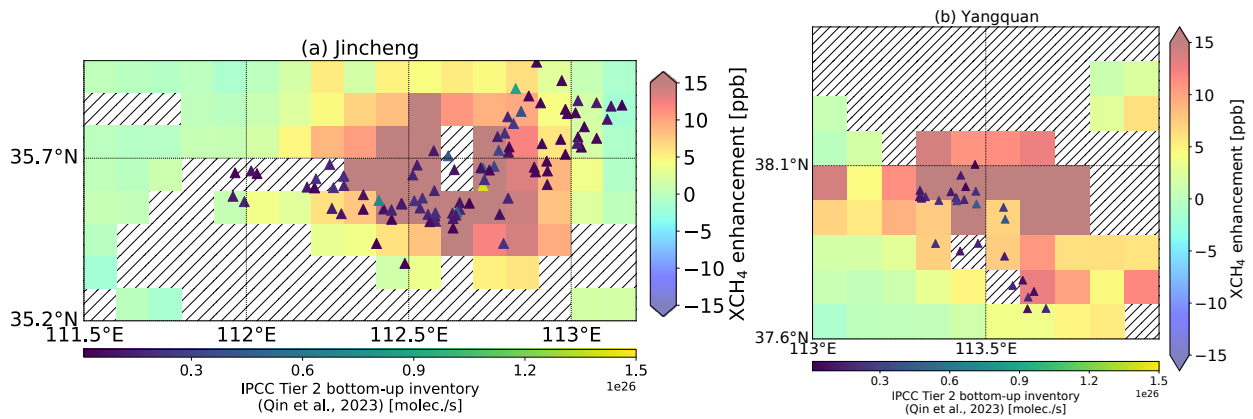


Figure A- 11: Similar to Figure A- 5(a) but for the grid at 36.5° N, 113° E in Changzhi.



480

Figure A- 12: XCH₄ enhancements (XCH₄ - background) for Jincheng and Yangquan region.

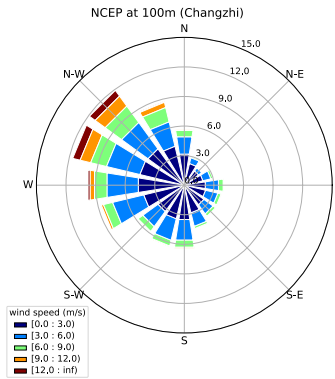
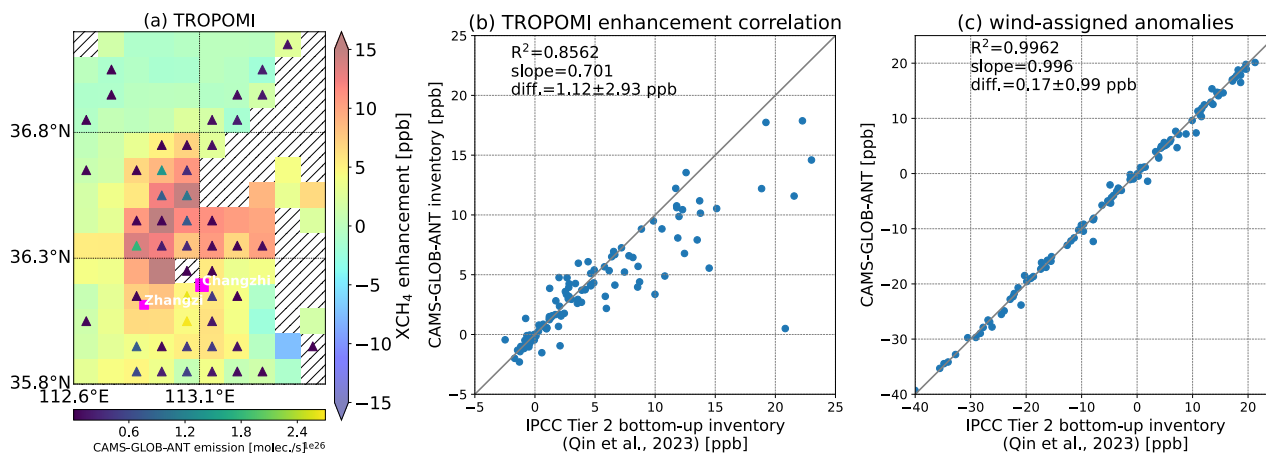


Figure A- 13: Similar to Figure A- 5(a) but from NCEP FNL operational analysis data in the Changzhi region.



485 **Figure A- 14: (a): similar** Similar to Figure 5(a) but using the CAMS-GLOB-ANT inventory as the ~~an~~ prior information. The triangle symbols denote the inventory location (emission rate $> 1 \times 10^{24}$ molec. s⁻¹). **(b): correlation between using the bottom-up inventory and the CAMS GLOB-ANT inventories for the modelled wind-assigned anomalies.** **(b): correlation for the enhancement and (c): correlation for the wind-assigned anomalies derived from the TROPOMI observations using the IPCC Tier 2 bottom-up inventory (Qin et al., 2023) and the CAMS-GLOB-ANT inventory. The grey line corresponds to the 1:1 line.**

490 References

Butz, A., Hasekamp, O. P., Frankenberg, C., and Aben, I.: Retrievals of atmospheric CO₂ from simulated space-borne measurements of backscattered near-infrared sunlight: accounting for aerosol effects, Appl. Opt., 48, 3322–3336, 2009.

495 Climate Change 2014: IPCC: Synthesis Report. Contribution of Working Groups I, II and III to the Fifth Assessment Report of the Intergovernmental Panel on Climate Change, edited by: Core Writing Team, Pachauri, R. K., and Meyer, L. A., IPCC, Geneva, Switzerland, 151 pp., 2014.

Crippa, M., Guizzardi, D., Solazzo, E., Muntean, M., Schaaf, E., Monforti-Ferrario, F., Banja, M., Olivier, J.G.J., Grassi, G., Rossi, S., Vignati, E., GHG emissions of all world countries - 2021 Report, EUR 30831 EN, Publications Office of the European Union, Luxembourg, 2021, ISBN 978-92-76-41547-3, doi:10.2760/173513, JRC126363.

500 Granier, C., Darras, S., Denier van der Gon, H., Doubalova, J., Elguindi, N., Galle, B., Gauss, M., Guevara, M., Jalkanen, J.-P., Kuenen, J., Lioussé, C., Quack, B., Simpson, D., and Sindelarova, K.: The Copernicus Atmosphere Monitoring Service global and regional emissions (April 2019 version), Copernicus Atmosphere Monitoring Service (CAMS) report, <https://doi.org/10.24380/d0bn-kx16>, 2019.

505 Liu, Y., Qin, K., Cohen, B. J., Kang, H. S., Hu, W., Lu, F., Wu, X. H, Yang, C. L. : Analysis of the characteristics of methane in the coal mining area of southeastern Shanxi with eddy and mobile observation, Journal of China Coal Society, 47(12): 4395-4402, 2022.

MEE, 2019a. The People's Republic of China Second Biennial Update Report on Climate Change, Ministry of Ecology and Environment of People's Republic of China. available at: <https://english.mee.gov.cn/Resources/Reports/reports/201907/P020190702568751604320.pdf> (last access: August 9, 2023), 2019a.

510 MEE, 2019b. The People's Republic of China Third National Communication on Climate Change, Ministry of Ecology and Environment of People's Republic of China, available at: <https://english.mee.gov.cn/Resources/Reports/reports/201907/P020190702566752327206.pdf> (last access: August 9, 2023), 2019b.

National Bureau of Statistics of China. China Statistical Yearbook 2017. Ch. 9 (China Statistics Press, Beijing, China, 2017).

515 National Centers for Environmental Prediction/National Weather Service/NOAA/U.S. Department of Commerce: NCEP GDAS/FNL 0.25 Degree Global Tropospheric Analyses and Forecast Grids, Research Data Archive at the National Center for Atmospheric Research, Computational and Information Systems Laboratory, <https://doi.org/10.5065/D65Q4T4Z> (last access: 19 August 2023), 2015.

520 NDRC, 2017. The People's Republic of China First Biennial Update Report on Climate Change National Development and Reform Commission.

NDRC: The National Development and Reform Commission: The People's Republic of China Initial National Communications on Climate Change National (SNCCCC), Development and Reform Commission, available at: <https://unfccc.int/sites/default/files/resource/China%20INC%20Chinese.pdf> (last access: August 9, 2023), 2004.

525 NDRC: The National Development and Reform Commission: The People's Republic of China Second National Communication on Climate Change National (SNCCCC), Development and Reform Commission, available at: <https://unfccc.int/resource/docs/natc/chnnc2e.pdf> (last access: August 9, 2023), 2012.

SACMS, Compilation of National Coal Mine Methane Level Identification for 2011 (Beijing: China University of Mining and Technology Press), 2012.

530 [Seinfeld, J.H., Pandis, S.N., Atmospheric Chemistry and Physics: From Air Pollution to Climate Changes. Wiley, New York, USA ISBN: 0-471-17815-2, 2006.](#)

UNFCCC, Greenhouse Gas Inventory Data Interface. https://di.unfccc.int/detailed_data_by_party. Last accessed 29 July 2023. 2021.

535 [Babenhauserheide, A., Hase, F., and Morino, I.: Net CO₂ fossil fuel emissions of Tokyo estimated directly from measurements of the Tsukuba TCCON site and radiosondes, Atmospheric Meas. Tech., 13, 2697–2710, <https://doi.org/10.5194/amt-13-2697-2020>, 2020.](#)

Butz, A., Guerlet, S., Hasekamp, O., Schepers, D., Galli, A., Aben, I., Frankenberg, C., Hartmann, J.-M., Tran, H., Kuze, A., Keppel-Aleks, G., Toon, G., Wunch, D., Wennberg, P., Deutscher, N., Griffith, D., Macatangay, R., Messerschmidt, J., Notholt, J., and Warneke, T.: Toward accurate CO₂ and CH₄ observations from GOSAT, *Geophys. Res. Lett.*, 38, <https://doi.org/10.1029/2011GL047888>, 2011.

540 [Chen, Z., Jacob, D. J., Nesser, H., Sulprizio, M. P., Lorente, A., Varon, D. J., Lu, X., Shen, L., Qu, Z., Penn, E., and Yu, X.: Methane emissions from China: a high-resolution inversion of TROPOMI satellite observations, Atmospheric Chem. Phys., 22, 10809–10826, <https://doi.org/10.5194/acp-22-10809-2022>, 2022.](#)

545 [Etminan, M., Myhre, G., Highwood, E. J., and Shine, K. P.: Radiative forcing of carbon dioxide, methane, and nitrous oxide: A significant revision of the methane radiative forcing, Geophys. Res. Lett., 43, 12,614–12,623, <https://doi.org/10.1002/2016GL071930>, 2016.](#)

- Foy, B. de, Schauer, J. J., Lorente, A., and Borsdorff, T.: Investigating high methane emissions from urban areas detected by TROPOMI and their association with untreated wastewater, *Environ. Res. Lett.*, 18, 044004, <https://doi.org/10.1088/1748-9326/acc118>, 2023.
- 550 Gao, J., Guan, C., and Zhang, B.: China's CH₄ emissions from coal mining: A review of current bottom-up inventories, *Sci. Total Environ.*, 725, 138295, <https://doi.org/10.1016/j.scitotenv.2020.138295>, 2020.
- Gao, J., Guan, C., Zhang, B., and Li, K.: Decreasing methane emissions from China's coal mining with rebounded coal production, *Environ. Res. Lett.*, 16, 124037, <https://doi.org/10.1088/1748-9326/ac38d8>, 2021.
- 555 de Gouw, J. A., Veeffkind, J. P., Roosenbrand, E., Dix, B., Lin, J. C., Landgraf, J., and Levelt, P. F.: Daily Satellite Observations of Methane from Oil and Gas Production Regions in the United States, *Sci. Rep.*, 10, 1379, <https://doi.org/10.1038/s41598-020-57678-4>, 2020.
- Guerlet, S., Butz, A., Schepers, D., Basu, S., Hasekamp, O. P., Kuze, A., Yokota, T., Blavier, J.-F., Deutscher, N. M., Griffith, D. W. T., Hase, F., Kyro, E., Morino, I., Sherlock, V., Sussmann, R., Galli, A., and Aben, I.: Impact of aerosol and thin cirrus on retrieving and validating XCO₂ from GOSAT shortwave infrared measurements, *J. Geophys. Res. Atmospheres*, 118, 4887–4905, <https://doi.org/10.1002/jgrd.50332>, 2013.
- 560 Hu, H., Landgraf, J., Detmers, R., Borsdorff, T., Aan de Brugh, J., Aben, I., Butz, A., and Hasekamp, O.: Toward Global Mapping of Methane With TROPOMI: First Results and Intersatellite Comparison to GOSAT, *Geophys. Res. Lett.*, 45, 3682–3689, <https://doi.org/10.1002/2018GL077259>, 2018.
- Janssens-Maenhout, G., Crippa, M., Guizzardi, D., Muntean, M., Schaaf, E., Dentener, F., Bergamaschi, P., Pagliari, V., Olivier, J. G. J., Peters, J. A. H. W., van Aardenne, J. A., Monni, S., Doering, U., Petrescu, A. M. R., Solazzo, E., and Oreggioni, G. D.: EDGAR v4.3.2 Global Atlas of the three major greenhouse gas emissions for the period 1970–2012, *Earth Syst. Sci. Data*, 11, 959–1002, <https://doi.org/10.5194/essd-11-959-2019>, 2019.
- 565 Li, M., Karu, E., Brenninkmeijer, C., Fischer, H., Lelieveld, J., and Williams, J.: Tropospheric OH and stratospheric OH and Cl concentrations determined from CH₄, CH₃Cl, and SF₆ measurements, *Npj Clim. Atmospheric Sci.*, 1, 1–7, <https://doi.org/10.1038/s41612-018-0041-9>, 2018.
- 570 Liu, G., Peng, S., Lin, X., Ciais, P., Li, X., Xi, Y., Lu, Z., Chang, J., Saunio, M., Wu, Y., Patra, P., Chandra, N., Zeng, H., and Piao, S.: Recent Slowdown of Anthropogenic Methane Emissions in China Driven by Stabilized Coal Production, *Environ. Sci. Technol. Lett.*, 8, 739–746, <https://doi.org/10.1021/acs.estlett.1c00463>, 2021.
- Lorente, A., Borsdorff, T., Butz, A., Hasekamp, O., aan de Brugh, J., Schneider, A., Wu, L., Hase, F., Kivi, R., Wunch, D., Pollard, D. F., Shiomi, K., Deutscher, N. M., Velasco, V. A., Roehl, C. M., Wennberg, P. O., Warneke, T., and Landgraf, J.: Methane retrieved from TROPOMI: improvement of the data product and validation of the first 2 years of measurements, *Atmospheric Meas. Tech.*, 14, 665–684, <https://doi.org/10.5194/amt-14-665-2021>, 2021.
- 575 Lu, Y. Y., Zhang, H. D., Zhou, Z., Ge, Z. L., Chen, C. J., Hou, Y. D., and Ye, M. L.: Current Status and Effective Suggestions for Efficient Exploitation of Coalbed Methane in China: A Review, *Energy Fuels*, 35, 9102–9123, <https://doi.org/10.1021/acs.energyfuels.1c00460>, 2021.
- 580 Maasackers, J. D., Jacob, D. J., Sulprizio, M. P., Scarpelli, T. R., Nesser, H., Sheng, J.-X., Zhang, Y., Hersher, M., Bloom, A. A., Bowman, K. W., Worden, J. R., Janssens-Maenhout, G., and Parker, R. J.: Global distribution of methane emissions, emission trends, and OH concentrations and trends inferred from an inversion of GOSAT satellite data for 2010–2015, *Atmospheric Chem. Phys.*, 19, 7859–7881, <https://doi.org/10.5194/acp-19-7859-2019>, 2019.

- 585 Miller, S. M., Michalak, A. M., Detmers, R. G., Hasekamp, O. P., Bruhwiler, L. M. P., and Schwietzke, S.: China's coal mine methane regulations have not curbed growing emissions, *Nat. Commun.*, 10, 303, <https://doi.org/10.1038/s41467-018-07891-7>, 2019.
- Pandey, S., Gautam, R., Houweling, S., van der Gon, H. D., Sadavarte, P., Borsdorff, T., Hasekamp, O., Landgraf, J., Tol, P., van Kempen, T., Hoogeveen, R., van Hees, R., Hamburg, S. P., Maasakkers, J. D., and Aben, I.: Satellite observations reveal extreme methane leakage from a natural gas well blowout, *Proc. Natl. Acad. Sci.*, 116, 26376–26381, <https://doi.org/10.1073/pnas.1908712116>, 2019.
- 590 Peng, S., Piao, S., Bousquet, P., Ciais, P., Li, B., Lin, X., Tao, S., Wang, Z., Zhang, Y., and Zhou, F.: Inventory of anthropogenic methane emissions in mainland China from 1980 to 2010, *Atmospheric Chem. Phys.*, 16, 14545–14562, <https://doi.org/10.5194/acp-16-14545-2016>, 2016.
- Plant, G., Kort, E. A., Murray, L. T., Maasakkers, J. D., and Aben, I.: Evaluating urban methane emissions from space using TROPOMI methane and carbon monoxide observations, *Remote Sens. Environ.*, 268, 112756, <https://doi.org/10.1016/j.rse.2021.112756>, 2022.
- 595 Qin, K., Hu, W., He, Q., Lu, F., and Cohen, J. B.: Individual Coal Mine Methane Emissions Constrained by Eddy-Covariance Measurements: Low Bias and Missing Sources, *EGU sphere*, 1–49, <https://doi.org/10.5194/egusphere-2023-1210>, 2023.
- Rigby, M., Montzka, S. A., Prinn, R. G., White, J. W. C., Young, D., O'Doherty, S., Lunt, M. F., Ganesan, A. L., Manning, A. J., Simmonds, P. G., Salameh, P. K., Harth, C. M., Mühle, J., Weiss, R. F., Fraser, P. J., Steele, L. P., Krummel, P. B., McCulloch, A., and Park, S.: Role of atmospheric oxidation in recent methane growth, *Proc. Natl. Acad. Sci.*, 114, 5373–5377, <https://doi.org/10.1073/pnas.1616426114>, 2017.
- 600 Sadavarte, P., Pandey, S., Maasakkers, J. D., Lorente, A., Borsdorff, T., Denier van der Gon, H., Houweling, S., and Aben, I.: Methane Emissions from Superemitting Coal Mines in Australia Quantified Using TROPOMI Satellite Observations, *Environ. Sci. Technol.*, 55, 16573–16580, <https://doi.org/10.1021/acs.est.1c03976>, 2021.
- 605 Saunio, M., Stavert, A. R., Poulter, B., Bousquet, P., Canadell, J. G., Jackson, R. B., Raymond, P. A., Dlugokencky, E. J., Houweling, S., Patra, P. K., Ciais, P., Arora, V. K., Bastviken, D., Bergamaschi, P., Blake, D. R., Brailsford, G., Bruhwiler, L., Carlson, K. M., Carrol, M., Castaldi, S., Chandra, N., Crevoisier, C., Crill, P. M., Covey, K., Curry, C. L., Etiope, G., Frankenberg, C., Gedney, N., Hegglin, M. I., Höglund-Isaksson, L., Hugelius, G., Ishizawa, M., Ito, A., Janssens-Maenhout, G., Jensen, K. M., Joos, F., Kleinen, T., Krummel, P. B., Langenfelds, R. L., Laruelle, G. G., Liu, L., Machida, T., Maksyutov, S., McDonald, K. C., McNorton, J., Miller, P. A., Melton, J. R., Morino, I., Müller, J., Murguia-Flores, F., Naik, V., Niwa, Y., Noce, S., O'Doherty, S., Parker, R. J., Peng, C., Peng, S., Peters, G. P., Prigent, C., Prinn, R., Ramonet, M., Regnier, P., Riley, W. J., Rosentreter, J. A., Segers, A., Simpson, I. J., Shi, H., Smith, S. J., Steele, L. P., Thornton, B. F., Tian, H., Tohjima, Y., Tubiello, F. N., Tsuruta, A., Viovy, N., Voulgarakis, A., Weber, T. S., van Weele, M., van der Werf, G. R., Weiss, R. F., 615 Worthy, D., Wunch, D., Yin, Y., Yoshida, Y., Zhang, W., Zhang, Z., Zhao, Y., Zheng, B., Zhu, Q., Zhu, Q., and Zhuang, Q.: The Global Methane Budget 2000–2017, *Earth Syst. Sci. Data*, 12, 1561–1623, <https://doi.org/10.5194/essd-12-1561-2020>, 2020.
- Scarpelli, T. R., Jacob, D. J., Maasakkers, J. D., Sulprizio, M. P., Sheng, J.-X., Rose, K., Romeo, L., Worden, J. R., and Janssens-Maenhout, G.: A global gridded ($0.1^\circ \times 0.1^\circ$) inventory of methane emissions from oil, gas, and coal exploitation based on national reports to the United Nations Framework Convention on Climate Change, *Earth Syst. Sci. Data*, 12, 563–575, <https://doi.org/10.5194/essd-12-563-2020>, 2020.
- 620 Schneising, O., Buchwitz, M., Reuter, M., Vanselow, S., Bovensmann, H., and Burrows, J. P.: Remote sensing of methane leakage from natural gas and petroleum systems revisited, *Atmospheric Chem. Phys.*, 20, 9169–9182, <https://doi.org/10.5194/acp-20-9169-2020>, 2020.

- 625 Shen, L., Jacob, D. J., Gautam, R., Omara, M., Scarpelli, T. R., Lorente, A., Zavala-Araiza, D., Lu, X., Chen, Z., and Lin, J.: National quantifications of methane emissions from fuel exploitation using high resolution inversions of satellite observations, *Nat. Commun.*, 14, 4948, <https://doi.org/10.1038/s41467-023-40671-6>, 2023.
- Sheng, J., Song, S., Zhang, Y., Prinn, R. G., and Janssens-Maenhout, G.: Bottom-Up Estimates of Coal Mine Methane Emissions in China: A Gridded Inventory, Emission Factors, and Trends, *Environ. Sci. Technol. Lett.*, 6, 473–478,
630 <https://doi.org/10.1021/acs.estlett.9b00294>, 2019.
- Tu, Q., Hase, F., Schneider, M., García, O., Blumenstock, T., Borsdorff, T., Frey, M., Khosrawi, F., Lorente, A., Alberti, C., Bustos, J. J., Butz, A., Carreño, V., Cuevas, E., Curcoll, R., Diekmann, C. J., Dubravica, D., Ertl, B., Estruch, C., León-Luis, S. F., Marrero, C., Morgui, J.-A., Ramos, R., Scharun, C., Schneider, C., Sepúlveda, E., Toledano, C., and Torres, C.: Quantification of CH₄ emissions from waste disposal sites near the city of Madrid using ground- and space-based observations of COCCON, TROPOMI and IASI, *Atmospheric Chem. Phys.*, 22, 295–317, <https://doi.org/10.5194/acp-22-295-2022>, 2022a.
635
- Tu, Q., Schneider, M., Hase, F., Khosrawi, F., Ertl, B., Necki, J., Dubravica, D., Diekmann, C. J., Blumenstock, T., and Fang, D.: Quantifying CH₄ emissions in hard coal mines from TROPOMI and IASI observations using the wind-assigned anomaly method, *Atmospheric Chem. Phys.*, 22, 9747–9765, <https://doi.org/10.5194/acp-22-9747-2022>, 2022b.
- Varon, D. J., McKeever, J., Jervis, D., Maasackers, J. D., Pandey, S., Houweling, S., Aben, I., Scarpelli, T., and Jacob, D. J.: Satellite Discovery of Anomalously Large Methane Point Sources From Oil/Gas Production, *Geophys. Res. Lett.*, 46, 13507–13516, <https://doi.org/10.1029/2019GL083798>, 2019.
640
- Veefkind, J. P., Aben, I., McMullan, K., Förster, H., de Vries, J., Otter, G., Claas, J., Eskes, H. J., de Haan, J. F., Kleipool, Q., van Weele, M., Hasekamp, O., Hoogeveen, R., Landgraf, J., Snel, R., Tol, P., Ingmann, P., Voors, R., Kruizinga, B., Vink, R., Visser, H., and Levelt, P. F.: TROPOMI on the ESA Sentinel-5 Precursor: A GMES mission for global observations of the atmospheric composition for climate, air quality and ozone layer applications, *Remote Sens. Environ.*, 120, 70–83, <https://doi.org/10.1016/j.rse.2011.09.027>, 2012.
645
- Zhang, Y., Gautam, R., Pandey, S., Omara, M., Maasackers, J. D., Sadavarte, P., Lyon, D., Nesser, H., Sulprizio, M. P., Varon, D. J., Zhang, R., Houweling, S., Zavala-Araiza, D., Alvarez, R. A., Lorente, A., Hamburg, S. P., Aben, I., and Jacob, D. J.: Quantifying methane emissions from the largest oil-producing basin in the United States from space, *Sci. Adv.*, <https://doi.org/10.1126/sciadv.aaz5120>, 2020.
650
- Zhang, Y., Jacob, D. J., Lu, X., Maasackers, J. D., Scarpelli, T. R., Sheng, J.-X., Shen, L., Qu, Z., Sulprizio, M. P., Chang, J., Bloom, A. A., Ma, S., Worden, J., Parker, R. J., and Boesch, H.: Attribution of the accelerating increase in atmospheric methane during 2010–2018 by inverse analysis of GOSAT observations, *Atmospheric Chem. Phys.*, 21, 3643–3666, <https://doi.org/10.5194/acp-21-3643-2021>, 2021.
- 655 [USDoS \(U.S. Department of State\). U.S.-China Joint Glasgow Declaration on Enhancing Climate Action in the 2020s. United States Department of State \(2021\). https://www.state.gov/u-s-china-joint-glasgow-declaration-on-enhancing-climate-action-in-the-2020s/ \(last access: 2023.12.21\)](https://www.state.gov/u-s-china-joint-glasgow-declaration-on-enhancing-climate-action-in-the-2020s/)